J. Fluid Mech. (2008), vol. 605, pp. 207–226.
doi:10.1017/S0022112008001493 Printed in the United Kingdom

Swinging and tumbling of elastic capsules in shear flow

S. KESSLER, R. FINKEN AND U. SEIFERT

II. Institut für Theoretische Physik, Universität Stuttgart, 70550 Stuttgart, Germany

(Received 27 June 2007 and in revised form 22 February 2008)

The deformation of an elastic micro-capsule in an infinite shear flow is studied numerically using a spectral method. The shape of the capsule and the hydrodynamic flow field are expanded into smooth basis functions. Analytic expressions for the derivative of the basis functions permit the evaluation of elastic and hydrodynamic stresses and bending forces at specified grid points in the membrane. Compared to methods employing a triangulation scheme, this method has the advantage that the resulting capsule shapes are automatically smooth, and few modes are needed to describe the deformation accurately. Computations are performed for capsules with both spherical and ellipsoidal unstressed reference shape. Results for small deformations of initially spherical capsules coincide with analytic predictions. For initially ellipsoidal capsules, recent approximate theories predict stable oscillations of the tank-treading inclination angle, and a transition to tumbling at low shear rate. Both phenomena have also been observed experimentally. Using our numerical approach we can reproduce both the oscillations and the transition to tumbling. The full phase diagram for varying shear rate and viscosity ratio is explored. While the numerically obtained phase diagram qualitatively agrees with the theory, intermittent behaviour could not be observed within our simulation time. Our results suggest that initial tumbling motion is only transient in this region of the phase diagram.

1. Introduction

The dynamics of soft objects such as drops, capsules and cells in flow represents a long-standing problem in science and engineering, but has received increasing interest recently, in particular due to its relevance to biological, medicinal and microfluidic applications. This problem is challenging from a theoretical point of view, because the shape of these objects is not given *a priori*, but determined dynamically from a balance of interfacial forces with fluid stresses. Improved experimental methods have revealed intriguing new dynamical shape transitions due to the presence of shear flow. The phenomenology of the dynamical behaviour depends distinctively on the specific soft object immersed in the flow, with fluid bilayer vesicles and elastic microcapsules as prominent classes.

Fluid bilayer vesicles assume a stationary tank-treading shape in linear shear flow, if there is no viscosity contrast between interior and exterior fluid (Kraus *et al.* 1996). If the interior fluid or the membrane becomes more viscous, a transition to a tumbling state can occur (Biben & Misbah 2003; Beaucourt *et al.* 2004*b*; Rioual, Biben & Misbah 2004; Noguchi & Gompper 2004, 2005; Vlahovska & Gracia 2007). Tank-treading was observed experimentally in infinite shear flow (de Haas *et al.* 1997; Kantsler & Steinberg 2005) and for vesicles interacting with a rigid wall

(Lorz *et al.* 2000; Abkarian, Lartigue & Viallat 2002), where a dynamic lift occurs (Seifert 1999*b*; Cantat & Misbah 1999; Sukumaran & Seifert 2001; Beaucourt, Biben & Misbah 2004*a*). The tank-treading to tumbling transition was observed convincingly for the first time in a recent experiment (Kantsler & Steinberg 2006). In addition to this transition, a vacillating or breathing motion was predicted theoretically (Misbah 2006) and observed experimentally (Kantsler & Steinberg 2006) and in simulations (Noguchi & Gompper 2007). The theoretical description has been expanded recently beyond first order in the shear rate (Lebedev, Turitsyn & Vergeles 2007).

In contrast to fluid vesicles, microcapsules exhibit a finite shear elasticity, since their membrane is chemically or physically cross-linked. This includes both artificial polymerised capsules (Walter, Rehage & Leonhard 2001) and red blood cells (RBCs), whose membrane is composed of an incompressible lipid bilayer over a thin elastic cytoskeleton (Mohandas & Evans 1994). The resistance to shear leads to qualitatively different behaviour, such as preventing the prolate to oblate shape transition in viscous fluid vesicles in channel flow (Noguchi & Gompper 2005). Perhaps most surprisingly, it also leads to qualitatively different instabilities such as wrinkling first observed experimentally on polymerised capsules (Walter *et al.* 2001), which should be distinguished from the transient creasing formation observed later on fluid vesicles (Kantsler, Segre & Steinberg 2007). The formation of the short-length-scale wrinkles is driven by compressive stress imposed on the membrane by the flow, while the selection of the short length scale is due to a balance between elastic stresses and bending forces (Finken & Seifert 2006).

When the unstressed initial shape of the cell is not spherical, material elements of the membrane are deformed when displaced from their initial position. This shape memory, suggested for RBCs by Fischer (2004), leads to a oscillation of the inclination angle superimposed on the tank-treading motion and an intermittent regime between tank-treading and tumbling (Skotheim & Secomb 2007; Abkarian, Faivre & Viallat 2007). For a review of the tank-treading behaviour of soft capsules in shear flow, see the first two chapters of Pozrikidis (2003*a*).

Analytic descriptions of the rather complex motion of capsules and vesicles is only possible for asymptotic cases, e.g. in the quasi-spherical limit (Barthès-Biesel 1980; Barthès-Biesel & Rallison 1981; Seifert 1999*a*; Misbah 2006; Finken & Seifert 2006; Lebedev *et al.* 2007; Vlahovska & Gracia 2007), or by restricting the number of degrees of freedom (Keller & Skalak 1982; Rioual *et al.* 2004; Skotheim & Secomb 2007). One therefore has to resort to numerical methods for more complex geometries.

For the dynamics of vesicles existing solvers which treat the flow at a continuum level either employ a discrete triangulation scheme (Kraus *et al.* 1996) or phase field models (Biben & Misbah 2003). An alternative route was taken by Noguchi & Gompper (2004, 2005), where the membrane is dynamically triangulated and the flow is modelled by discrete effective fluid particles.

Numerical simulations of capsules were first performed in an axisymmetric geometry (Li, Barthès-Biesel & Helmy 1988; Leyrat-Maurin, Drochon & Barthès-Biesel 1993; Leyrat-Maurin & Barthes-Biesel 1994). Pozrikidis (1995) developed a method for simulating three-dimensional deformations of initially spherical capsules in shear flow using a boundary element formulation. This method was later refined by Ramanujan & Pozrikidis (1998), who also observed oscillations of the inclination angle for ellipsoidal capsules. However, their method was plagued by numerical instabilities for high and low deformations due to the degradation of the grid. Further improvement of the boundary element method allows the stable simulation of tank-treading and tumbling motion of highly flattened capsules only by numerically smoothing the surface (Pozrikidis 2003*b*). Part of the numerical difficulties might be due to the evaluation of bending moments: calculating the local mean curvature requires taking second derivatives of the shape functions, which become inaccurate using finite difference schemes. Newer approaches, such as the spectral boundary algorithms proposed for droplets (Wang & Dimitrakopoulos 2006) and solid particles (Pozrikidis 2006), therefore use higher-order basis functions on the triangulated surface. While these methods are very versatile, the details are rather complex. Suitable interfacial smoothing is still needed to ensure numerical stability of the method (Wang & Dimitrakopoulos 2006).

It is therefore the purpose of this paper to augment these approaches with a global spectral method. In this method the shape of the capsule is expanded into a set of smooth basis functions (Boyd 2001). This has the advantage that the resulting shape is automatically globally smooth, which reduces the discretization error, especially in higher derivatives such as the local mean curvature. Since the derivatives of the basis functions are analytically known, it is easy to evaluate the elastic tensions and bending moments at a grid of collocation points. These marker points are material points of the underlying connected membrane. Rather than treating the hydrodynamics in a boundary layer formulation, we expand the Stokes flow similarly in terms of smooth basis functions. Requiring force balance at the collocation points yields the equation of motion of the membrane. This scheme is used to systematically explore the dynamic behaviour of capsules in shear flow, focusing on initially non-spherical capsules as considered in the analysis by Skotheim & Secomb (2007). Although the overall phase behaviour of the capsules is captured qualitatively by their model, we could not observe the predicted intermittent behaviour. An analysis of the capsule dynamics suggests that the initial tumbling motion is only a transient towards a stable tank-treading motion.

This paper is organized as follows. In § 2, after introducing notions of differential geometry and elasticity, we define the problem rigorously. In § 3, we develop the spectral algorithm to calculate the dynamics of an elastic capsule. After extensive testing for analytically known limit cases in § 4, we apply our method to ellipsoidal capsules in § 5. Our findings are summarized in § 6. In the Appendix, we recall the relevant differential geometry for deformed capsules.

2. Problem formulation

We consider the dynamics of a closed capsule that is embedded in an infinite ambient flow with viscosity η^{o} (see figure 1). The elastic membrane encloses a second fluid with a different viscosity η^{i}, defining the dimensionless viscosity contrast

$$\epsilon \equiv \eta^{\mathrm{i}}/\eta^{\mathrm{o}} . \tag{2.1}$$

In the absence of the capsule we assume a prescribed external flow $\boldsymbol{u}^{\infty}(\boldsymbol{x})$. Because of its small thickness we consider the membrane as a two-dimensional interface that separates the two fluids. On the typical length scales considered inertial effects of the membrane are negligible.

Strain and curvature

In order to describe the two-dimensional membrane, which is embedded in three-dimensional space, we recall some important terms of differential geometry (Frankel 2004; Marsden & Hughes 1983). For mathematical details of the quantities used here,

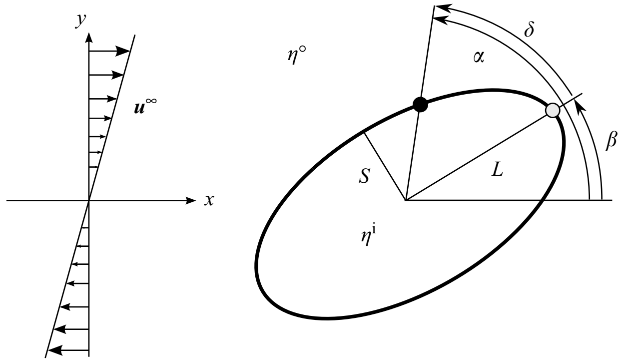

FIGURE 1. Elastic capsule in hydrodynamic flow. The viscosity of the outer flow and the inner fluid are η^o and η^i, respectively. Long and short axes of the deformed capsule are denoted by L and S. The inclination angle β measures the angle between the direction of maximal elongation and that of the shear flow $\boldsymbol{u}^\infty = \dot{\gamma} y \boldsymbol{e}_x$. The angle defined by a tracer particle on the membrane compared to the flow direction is denoted by α.

see the Appendix. A comprehensive summary of interfacial properties in the context of membranes in hydrodynamic flow can be found in Pozrikidis (2001).

Since we consider closed membranes with the topology of a sphere S^2, we can label the material points of some reference membrane by spherical coordinates (ϑ, φ). Note that for an arbitrarily deformed membrane the material point labelled by the Lagrange coordinates (ϑ, φ) will be moved, and (ϑ, φ) will not remain spherical coordinates.

The location of the membrane $\mathscr{M}$ at time t is given by the shape function $\boldsymbol{r}(\vartheta, \varphi; t)$. Length and angles on the membrane are measured by the first fundamental form or metric tensor $\boldsymbol{g}$ with covariant components g_{ij} (A 3). The second fundamental form or extrinsic curvature tensor $\boldsymbol{k}$ with covariant components k_{ij} (A 8) measures how the unit normal vector of the surface changes its direction, on moving along the membrane. The mean curvature H is defined as the arithmetic mean of the principle curvatures, which are both the eigenvalues of the curvature tensor $\boldsymbol{k}$ and the inverse of the principle curvature radii (A 9). In our convention (A 8), the mean curvature $H = 2/r$ of a sphere with radius r is positive. First and second fundamental forms completely fix the shape of the given membrane and therefore contain all the information about the membrane shape.

In order to describe a deformation and an elastic response, we have to specify an unstressed reference membrane $\mathscr{M}_{\mathrm{ref}}$ given by the shape function $\boldsymbol{R}(\vartheta, \varphi)$. The corresponding metric is denoted by $\boldsymbol{G}$ and defined analogously to the metric tensor $\boldsymbol{g}$. The Lagrangian strain tensor $\boldsymbol{\varepsilon}$, is, in covariant components ε_{ij}, given by half the difference of metric g_{ij} and reference metric G_{ij} (A 10) and measures the change in length elements of the membrane upon deformation (Marsden & Hughes 1983), and Appendix. The strain tensor $\boldsymbol{\varepsilon}$ holds all the information about the deformation and will be used to define an elastic energy density.

Finally, the surface dilation J (A 11) measures how an infinitesimal patch of area $\mathrm{d}A$ on the reference membrane is changed upon deformation into the patch of area $\mathrm{d}a$ (A 7) and can be expressed by the ratio of determinants of deformed and reference metrics (A 5).

Constitutive laws, energy, force, stress

The deformation of the membrane from its unstressed shape costs energy, which can be quantified by the underlying constitutive law. In general we consider resistance against shear, dilation, and bending. Several elastic models for thin shells and membranes are considered in the literature. A short overview is found in Barthès-Biesel, Diaz & Dhenin (2002) and in the first two chapters of Pozrikidis (2003*a*). These references directly connect the deformation with stresses and bending moments. We prefer to derive the constitutive law from the elastic energy, as outlined in Marsden & Hughes (1983).

Deformation from the reference shape $\boldsymbol{R}(\vartheta, \varphi)$ to a shape $\boldsymbol{r}(\vartheta, \varphi; t)$ costs energy $\mathscr{H}[\boldsymbol{r}]$. We only consider constitutive laws derived from an energy density $h[\boldsymbol{r}]$, i.e.

$$\mathscr{H}[\boldsymbol{r}] = \int_{\mathscr{M}_{\mathrm{ref}}} \mathrm{d}A \, h[\boldsymbol{r}] \,. \tag{2.2}$$

Variation of the shape $\boldsymbol{r}$ by $\delta\boldsymbol{r}$ while leaving the reference shape fixed induces a variation of the total free energy

$$\delta\mathscr{H} = \int_{\mathscr{M}_{\mathrm{ref}}} \mathrm{d}A \, \frac{\delta\mathscr{H}[\boldsymbol{r}]}{\delta\boldsymbol{r}} \cdot \delta\boldsymbol{r} \equiv -\int_{\mathscr{M}} \mathrm{d}a \, \boldsymbol{f} \cdot \delta\boldsymbol{r} \,, \tag{2.3}$$

which defines the elastic surface force density $\boldsymbol{f}$ on the membrane by a functional derivative

$$\boldsymbol{f} \equiv -\frac{1}{J} \frac{\delta\mathscr{H}[\boldsymbol{r}]}{\delta\boldsymbol{r}} \,. \tag{2.4}$$

We now specialize to deformation energies, which can be written as the sum of a purely elastic and a bending part,

$$\mathscr{H}[\boldsymbol{r}] = \mathscr{H}_{\mathrm{el}}[\boldsymbol{r}] + \mathscr{H}_{\kappa}[\boldsymbol{r}] \,. \tag{2.5}$$

To illustrate the method, we use the specific constitutive law for the elastic free energy

$$\mathscr{H}_{\mathrm{el}} = \int_{\mathscr{M}_{\mathrm{ref}}} \mathrm{d}A \left(\frac{\lambda + 2\mu}{2} (\mathrm{tr}\,\boldsymbol{\varepsilon})^2 + 2\mu \det \boldsymbol{\varepsilon} \right) , \tag{2.6}$$

and the curvature term (Helfrich 1973)

$$\mathscr{H}_{\kappa} = \int_{\mathscr{M}} \mathrm{d}a \frac{\kappa}{2} (2H - C_0)^2 = \int_{\mathscr{M}_{\mathrm{ref}}} \mathrm{d}A \, J \frac{\kappa}{2} (2H - C_0)^2 \tag{2.7}$$

for the bending energy. Here, κ is the bending rigidity and C_0 is the spontaneous curvature, while λ and μ are the 2d-Lamé coefficients in Hooke's law valid for small deformations. These coefficients correspond to the surface shear modulus $G_s = \mu$ and the surface Poisson ratio $\nu_s = \lambda/(\lambda + 2\mu)$ in the notation of Barthès-Biesel *et al.* (2002). Other constitutive laws can trivially be implemented.

Hydrodynamics

For all experimental setups the Reynolds number is small and the flow is governed by the linear Stokes equations. The velocity $\boldsymbol{u}^{\alpha}(\boldsymbol{x})$ of the inner ($\alpha = \mathrm{i}$) and outer ($\alpha = \mathrm{o}$) fluid at the position $\boldsymbol{x}$ is determined by the incompressibility relation

$$\nabla \cdot \boldsymbol{u}^{\alpha} = 0 \,, \tag{2.8}$$

the linear momentum equation

$$-\nabla p^{\alpha} + \eta^{\alpha} \Delta \boldsymbol{u}^{\alpha} = \boldsymbol{0} \tag{2.9}$$

with the isotropic pressure p^α, and by appropriate boundary conditions far away from the capsule and at the membrane.

The flow must be regular everywhere and continuous across the membrane when assuming a no-slip boundary condition. The jump in hydrodynamic traction between both fluids is compensated by the elastic forces at the membrane

$$\boldsymbol{f}(\vartheta,\varphi) = \left[\boldsymbol{T}^{\mathrm{i}}(\boldsymbol{r}(\vartheta,\varphi)) - \boldsymbol{T}^{\mathrm{o}}(\boldsymbol{r}(\vartheta,\varphi))\right] \cdot \boldsymbol{n}(\vartheta,\varphi), \tag{2.10}$$

where $\boldsymbol{T}^\alpha$ is the inner and outer hydrodynamic stress tensor with Cartesian components

$$T_{ij}^\alpha \equiv -\delta_{ij} p^\alpha + \eta^\alpha \left(\partial_i u_j^\alpha + \partial_j u_i^\alpha\right) . \tag{2.11}$$

Since we are assuming no-slip boundary conditions, the velocity is continuous across the membrane, and the membrane is advected with the flow

$$\boldsymbol{u}^{\mathrm{i}}(\boldsymbol{x})\big|_{\boldsymbol{x}=\boldsymbol{r}(\vartheta,\varphi;t)} = \boldsymbol{u}^{\mathrm{o}}(\boldsymbol{x})\big|_{\boldsymbol{x}=\boldsymbol{r}(\vartheta,\varphi;t)} = \partial_t \boldsymbol{r}(\vartheta,\varphi;t). \tag{2.12}$$

Far away from the capsule the outer flow coincides with the undisturbed external flow $\boldsymbol{u}^\infty$

$$\boldsymbol{u}^{\mathrm{o}}(\boldsymbol{x}) \to \boldsymbol{u}^\infty(\boldsymbol{x}) \quad \text{for } |\boldsymbol{x}| \to \infty. \tag{2.13}$$

Since the Stokes equations are linear, we can split the total flow into a sum of the undisturbed flow and an induced flow

$$\boldsymbol{u}^\alpha \equiv \boldsymbol{u}^\infty + \boldsymbol{u}_{\mathrm{ind}}^\alpha , \tag{2.14}$$

where the homogeneous boundary condition $\boldsymbol{u}_{\mathrm{ind}}^\alpha(\boldsymbol{x}) \to 0$ far away from the capsule is easy to implement.

For specific applications, we employ a linear shear flow (figure 1)

$$\boldsymbol{u}^\infty(\boldsymbol{x}) = \dot{\gamma}\, y \boldsymbol{e}_x \tag{2.15}$$

with shear rate $\dot{\gamma}$. The equations of motion of the membrane are fully determined by Stokes' equations (2.8), (2.9), the force balance with the elastic forces (2.10), and the boundary conditions (2.12), (2.13) which include the membrane advection (right-hand side of 2.12).

Dimensionless parameters

The motion of the capsule is governed by a number of dimensionless parameters: The volume V of the capsule remains constant and defines a length scale R_0

$$V \equiv \frac{4\pi}{3} R_0^3 , \tag{2.16}$$

which will be used as the unit length. The elastic energy density is given by the elastic moduli depending on the given constitutive law. In our case we use the shear elasticity μ to define an energy scale μR_0^2. The remaining elastic parameters can thus be cast in a non-dimensional form by defining the two-dimensional Poisson number

$$\nu \equiv \frac{\lambda}{\lambda + 2\mu}, \tag{2.17}$$

the non-dimensional bending rigidity

$$\tilde{\kappa} \equiv \frac{\kappa}{\mu R_0^2}, \tag{2.18}$$

and spontaneous curvature

$$\tilde{C}_0 \equiv \frac{R_0}{2} C_0 . \tag{2.19}$$

The viscosity η^{o} can be used to define a time scale $R_0\eta^{\mathrm{o}}/\mu$, giving the capillary number

$$\chi \equiv \frac{R_0\eta^{\mathrm{o}}}{\mu}\dot{\gamma} . \tag{2.20}$$

Finally, the viscosity contrast ϵ has already been defined in (2.1).

3. Spectral method

We now develop a method to numerically solve the nonlinear equations of motion.

Spectral method

To transform the shape function to spectral space, we expand its Cartesian components $r^i(\vartheta, \varphi) \equiv \boldsymbol{r}(\vartheta, \varphi)\cdot\boldsymbol{e}_i$ into scalar spherical harmonics $Y_l^m(\vartheta, \varphi)$ with $l \geqslant 0, |m| \leqslant l$ (Rose 1957; Brink & Satchler 1968). More generally, we consider the spectral expansion of a scalar function f

$$f(\vartheta, \varphi) = \sum_{lm} f^{lm} Y_l^m(\vartheta, \varphi) . \tag{3.1}$$

Since the set of all spherical harmonics form a complete and orthonormal basis on the sphere S^2:

$$\int_{S^2} \mathrm{d}\omega\, Y_l^{*m}(\vartheta, \varphi) Y_{l'}^{m'}(\vartheta, \varphi) = \delta_{mm'}\delta_{ll'} , \tag{3.2}$$

the spectral coefficients are in principle obtained by the integral

$$f^{lm} = \int_{S^2} \mathrm{d}\omega\, Y_l^{*m}(\vartheta, \varphi) f(\vartheta, \varphi) . \tag{3.3}$$

Here $\mathrm{d}\omega = \sin\vartheta\ \mathrm{d}\vartheta\ \mathrm{d}\varphi$ denotes the area element on the sphere S^2 and the superscript star indicates the complex conjugate. For numerical applications, however, this integral must be replaced by a discrete sum. For the hydrodynamic part it will be useful to extend the spherical harmonics to $l < 0$ by defining $Y_{-(l+1)}^m \equiv Y_l^m$.

A function whose spectral coefficients f^{lm} vanish for $l \geqslant b$ is called a band-limited function with band limit b (Healy *et al.* 2003). We solve the dynamics of the membrane by restricting to the space of band-limited shape functions. Since the spectral amplitude of smooth functions decays exponentially with l (Boyd 2001), this scheme is already very accurate for low b.

To obtain the expansion coefficients out of a given band-limited function, we choose a finite number of collocation markers (ϑ_i, φ_i), $i = 1, \ldots, n$ at the membrane. A scalar function $f(\vartheta, \varphi)$ on the membrane is then determined by its values at these points $f_i \equiv f(\vartheta_i, \varphi_i)$, whereas in spectral space this function is represented by the spectral coefficients f^{lm} up to the bandwidth b. Transformation from spectral space to real space is easily done by evaluating the spherical harmonics at the collocation points

$$f_i = \sum_{lm} f^{lm} Y_l^m(\vartheta_i, \varphi_i) \equiv \sum_{lm} A_i^{lm} f^{lm} . \tag{3.4}$$

If the transformation matrix A_i^{lm} is square and regular, the inverse transformation can be obtained by

$$f^{lm} = \sum_i f_i (\boldsymbol{A}^{-1})_i^{lm} , \tag{3.5}$$

where $\boldsymbol{A}^{-1}$ is the inverse of $\boldsymbol{A}$. However, often more collocation points than spectral modes are used (Healy *et al.* 2003): a natural choice is to define the collocation markers $i \equiv (j, k)$ equidistantly in ϑ and φ, where we shift the values of ϑ away from the poles to avoid numerical problems in the vicinity of the pole (Boyd 2001)

$$\vartheta_{(j,k)} \equiv \frac{(2j+1)\pi}{4b} , \tag{3.6}$$

$$\varphi_{(j,k)} \equiv \frac{k\pi}{b} , \tag{3.7}$$

with $j, k = 0, \ldots, 2b-1$. With this choice the number of markers $n = 4b^2$ is larger than the number of spectral modes b^2. In this case $\boldsymbol{A}^{-1}$ must be replaced by the Moore-Penrose-Pseudoinverse (Swarztrauber & Spotz 2004).

The expressions for the metric and curvature involve first-order and second-order derivatives, respectively. The main advantage of spectral methods is that the derivatives of the basis functions are known algebraically (Rose 1957; Brink & Satchler 1968), and therefore differentiation can be performed with high accuracy for band-limited functions. Similarly, the integral over the function f is evaluated numerically via

$$\int_{S^2} \mathrm{d}\omega\, f(\vartheta, \varphi) = \sqrt{4\pi} f^{00} , \tag{3.8}$$

which follows easily from $Y_0^0(\vartheta, \varphi) = 1/\sqrt{4\pi}$. Once the derivatives of the shape functions are known, all further geometrical computations are performed at the collocation points in physical space. It is straightforward to numerically calculate the energy density of a given shape for a given constitutive law with high accuracy. Similarly, the variation of the energy density is evaluated for a given shape and variation of the shape function.

Elastic forces

To obtain the force density at the collocation points, we need to calculate the variation of the total free energy for special variations of the shape. The spectral coefficients of the force density are obtained in the most direct way when we choose the specific variations

$$\delta \boldsymbol{r}_i^{lm}(\vartheta, \varphi) \equiv -\frac{\sin\vartheta}{\sqrt{g(\vartheta, \varphi)}} Y_l^{*m}(\vartheta, \varphi) \boldsymbol{e}_i , \quad l = 0, \ldots, b ; \quad m = -l, \ldots, l ; \quad i = x, y, z. \tag{3.9}$$

The variation of the metric and curvature tensor resulting from this shape variation can be evaluated easily using the known derivatives of the shape function. Since the derivatives of the energy density with respect to metric and curvature are known analytically, the variation of the elastic energy (2.3) can be calculated easily. For the specific choice of $\delta \boldsymbol{r}_i^{lm}$ (3.9), this yields directly the Cartesian spectral force components

$$\delta \mathscr{H} = -\int_{\mathscr{M}} \mathrm{d}a\, \boldsymbol{f} \cdot \delta \boldsymbol{r}_i^{lm} = \int_{S^2} \mathrm{d}\omega\, \boldsymbol{f} \cdot \boldsymbol{e}_i Y_l^{*m}(\vartheta, \varphi) = f_i^{lm}. \tag{3.10}$$

Hydrodynamics

We follow a similar strategy for the hydrodynamic part of the problem. To solve the hydrodynamic equations, we choose a complete set of basis functions in three-dimensional space that automatically fulfil Stokes' equations. These so-called Lamb modes (Lamb 1932; Happel & Brenner 1983) can be defined as appropriate linear combinations of vector spherical harmonics. Spherical coordinates r, θ and ϕ in the laboratory frame as well as the corresponding basis vectors $\boldsymbol{e}_r$, $\boldsymbol{e}_\theta$ and $\boldsymbol{e}_\phi$ are best suited for calculations concerning the Lamb modes. We stress again the difference between the Lagrangian coordinates (ϑ, φ), which serve as markers for the material points, and the angles (θ, ϕ), which are spherical coordinates in the laboratory frame. With help of the surface gradient on the sphere S^2

$$\nabla^{\mathrm{S}} \equiv \boldsymbol{e}_\theta \partial_\theta + \frac{1}{\sin\theta} \boldsymbol{e}_\phi \partial_\phi \tag{3.11}$$

the vector spherical harmonics are given by (Morse & Feshbach 1953)

$$\boldsymbol{Y}_l^m(\theta, \phi) \equiv Y_l^m(\theta, \phi) \boldsymbol{e}_r \,, \tag{3.12}$$

$$\boldsymbol{\Psi}_l^m(\theta, \phi) \equiv \frac{1}{\sqrt{l(l+1)}} \nabla^{\mathrm{S}} Y_l^m(\theta, \phi) \,, \tag{3.13}$$

$$\boldsymbol{\Phi}_l^m(\theta, \phi) \equiv \frac{1}{\sqrt{l(l+1)}} \boldsymbol{e}_r \times \nabla^{\mathrm{S}} Y_l^m(\theta, \phi) \,. \tag{3.14}$$

The Lamb modes then are

$$\boldsymbol{U}_{l,m}^{p}(\theta, \phi) \equiv \frac{1}{2(l+1)(2l+3)} \left[l(l+1) \boldsymbol{Y}_l^m(\theta, \phi) + (l+3)\sqrt{l(l+1)} \boldsymbol{\Psi}_l^m(\theta, \phi) \right] , \tag{3.15}$$

$$\boldsymbol{U}_{l,m}^{\phi}(\theta, \phi) \equiv l \boldsymbol{Y}_l^m(\theta, \phi) + \sqrt{l(l+1)} \boldsymbol{\Psi}_l^m(\theta, \phi) \,, \tag{3.16}$$

$$\boldsymbol{U}_{l,m}^{\chi}(\theta, \phi) \equiv -\sqrt{l(l+1)} \boldsymbol{\Phi}_l^m(\theta, \phi) \,. \tag{3.17}$$

With the scalar spherical harmonics and the Lamb modes as basis functions the pressure and velocity fields can be expanded for the external and internal as well as the induced flow

$$p^\alpha(r, \theta, \phi) = \eta^\alpha \sum_{lm} p_{l,m}^\alpha r^l Y_l^m(\theta, \phi) \,, \tag{3.18}$$

$$\boldsymbol{u}^\alpha(r, \theta, \phi) = \sum_{lm} \left(p_{l,m}^\alpha r^{l+1} \boldsymbol{U}_{l,m}^{p}(\theta, \phi) + \phi_{l,m}^\alpha r^{l-1} \boldsymbol{U}_{l,m}^{\phi}(\theta, \phi) + \chi_{l,m}^\alpha r^l \boldsymbol{U}_{l,m}^{\chi}(\theta, \phi) \right) . \tag{3.19}$$

Owing to the regularity of the induced flow at the origin and the boundary conditions at infinity (2.13), the sums are restricted to $l \geqslant 0$ for $\boldsymbol{u}_{\mathrm{ind}}^{\mathrm{i}}$ and $l \leqslant -2$ for $\boldsymbol{u}_{\mathrm{ind}}^{\mathrm{o}}$.

The remaining boundary conditions (2.12) and force balance condition (2.10) result in linear equations for the coefficients of the Lamb modes. For our choice of collocation points, we have an overdetermined system that can be solved in a least-square sense. In this way we obtain the hydrodynamic flow for any given deformation of the capsule.

Since the capsule is simply advected with the flow (2.12), we perform Euler steps with a sufficently small time step to determine the dynamics of the capsule. Higher-order methods such as a second-order Runge–Kutta have been tested, but did not yield significant improvements in terms of stability and overall simulation time.

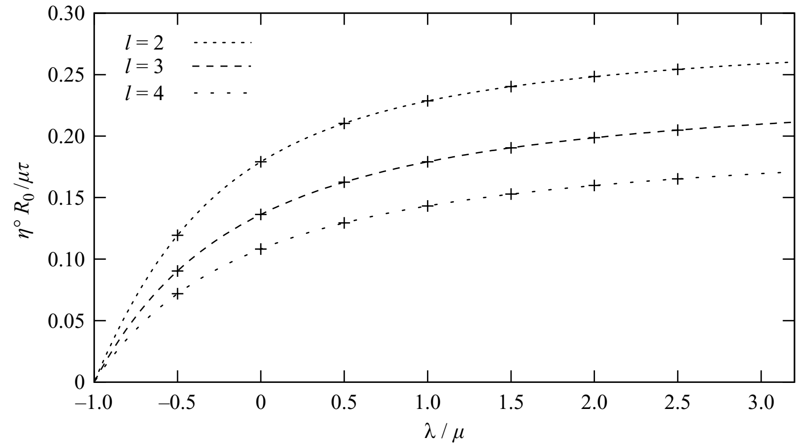

FIGURE 2. Comparison of numerically and analytically obtained relaxation time. The symbols show numerically obtained values of the scaled inverse relaxation time $\eta^o R_0/\mu\tau$ of bending modes as a function of the ratio λ/μ for different harmonic indexes $l = 2$, $l = 3$, $l = 4$ and $\kappa = 0$. The curves are the analytic solution of the secular equation (24) of Rochal *et al.* (2005).

4. Spherical capsules

To test our method, we compare with quasi-spherical results that can be obtained analytically. These tests comprise the relaxation dynamics of a capsule to its spherical reference shape in quiescent fluid and the stationary deformation of a capsule in linear shear flow for low shear rates.

Small deformations of an initially spherical capsule relax exponentially in time. Rochal, Lorman & Mennessier (2005) have identified the normal modes, and calculated the corresponding relaxation times. The relaxation modes are linear combinations of vector spherical harmonics and are likewise labelled by l, m. For each set of angular momentum numbers, three relaxation normal modes exist, which have been termed ‘stretching’, ‘bending’, and ‘shear’ modes, respectively. The corresponding relaxation times are obtained from the eigenvalue equation (24) of Rochal *et al.* (2005).

As a numerical test of our code, a spherical capsule was deformed in the direction of a normal mode, and the time constant of the subsequent relaxation to equilibrium was extracted. In figure 2, we compare the relaxation times of selected modes as a function of the Lamé parameter λ with the theoretical predictions, with excellent agreement.

Switching on the shear flow with a low shear rate, the capsule relaxes into a stationary shape with a tank-treading motion. The stationary deformations have been calculated to first and second order in the deformation by Barthès-Biesel & Rallison (1981). The deformation of the capsule is measured by the time-dependent Taylor deformation parameter

$$D \equiv \frac{L - S}{L + S}, \tag{4.1}$$

where L is the longest and S is the shortest distance of the membrane from the centre (see figure 1). In the long time limit, D assumes a stationary value D_0, which is to first order in χ ($\tilde{C}_0 = 1$)

$$D_0 \approx \frac{5}{4}\frac{\nu+2}{\nu+1+2\tilde{\kappa}(\nu+5)}\chi = \frac{5}{8}\frac{(4\mu+3\lambda)R_0\eta^{\circ}}{(\mu+\lambda)\mu+\left(2\kappa/R_0^2\right)(3\lambda+5\mu)}\dot{\gamma}\,. \tag{4.2}$$

In our simulations, the unstressed capsule is subjected to an abruptly started linear shear flow. Numerically, the deformation and inclination are not calculated directly according to definition (4.1). As described by Ramanujan & Pozrikidis (1998), we find it more suitable to use instead the deformation parameter of an ellipsoid with the same tensor of inertia. In the small deformation limit, both definitions are equivalent.

The simulations were performed by using a bandwidth of $b = 11$ corresponding to 121 modes, and a total of $N = 4b^2 = 484$ grid points. The bending energy was chosen to prevent the formation of wrinkling modes within the bandwidth. The time step was chosen small enough to yield a stable evolution. Typical values were $\Delta t \sim 1/(1000\dot{\gamma})$. The time evolution of the deformation parameter of an initially spherical capsule is shown in figure 3 for different shear rates and fixed elastic parameters. To illustrate the stationary tank-treading motion of the capsule, we also show the distance of a marker point on the membrane from the centre of the capsule as a function of time. This distance oscillates with twice the tank-treading frequency between L and S. At low shear rate, we observe a monotonic relaxation of the deformation to its stationary value D_0, while for large χ and ϵ a pronounced over-shoot is observed (cf. Ramanujan & Pozrikidis 1998). The numerical deformation D_0 clearly follows the asymptotic prediction (4.2) for low shear rate. For large shear rates, the simulation data show deviations from linear behaviour. These are probably due to the rotational part of the linear shear flow, since for non-zero vorticity the stationary deformation is a nonlinear function of the shear rate even in the quasi-spherical limit.

5. Ellipsoidal capsules

After successfully testing our spectral method by means of a spherical initial or reference shape, we can investigate the dynamics of capsules with an ellipsoidal initial shape. This case is both experimentally more realistic, since synthesised capsules are never perfectly spherical, and leads to a richer dynamical behaviour of the capsules. In a non-spherical reference shape, the membrane points are no longer equivalent to each other. During the course of a tank-treading motion, a membrane element is therefore periodically deformed, which costs elastic energy. Any membrane element therefore energetically prefers its initial position (or one of the equivalent positions by symmetry of the reference shape). This effect is called 'shape memory', and also plays an important role in the dynamics of red blood cells (Fischer 2004; Watanabe *et al.* 2006).

The shape memory effect is the cause of oscillations of the deformation and the inclination angle in the tank-treading state, as observed experimentally by Chang & Olbricht (1993), Walter *et al.* (2001), and Abkarian *et al.* (2007), and also found in the simulations by Ramanujan & Pozrikidis (1998). Recently, a modified Keller–Skalak type theory was proposed (Skotheim & Secomb 2007), which explains this behaviour qualitatively. Their model also predicts an oscillating tank-treading motion at large shear rate, and a tumbling motion at lower shear rate. In the tumbling regime, a tracer particle on the membrane oscillates around a fixed position with respect to the capsule shape. In the intermediate shear rate regime, intermittent motion, which alternates between tumbling and tank-treading, is predicted. Although direct experimental evidence for this behaviour is missing, indirect evidence was

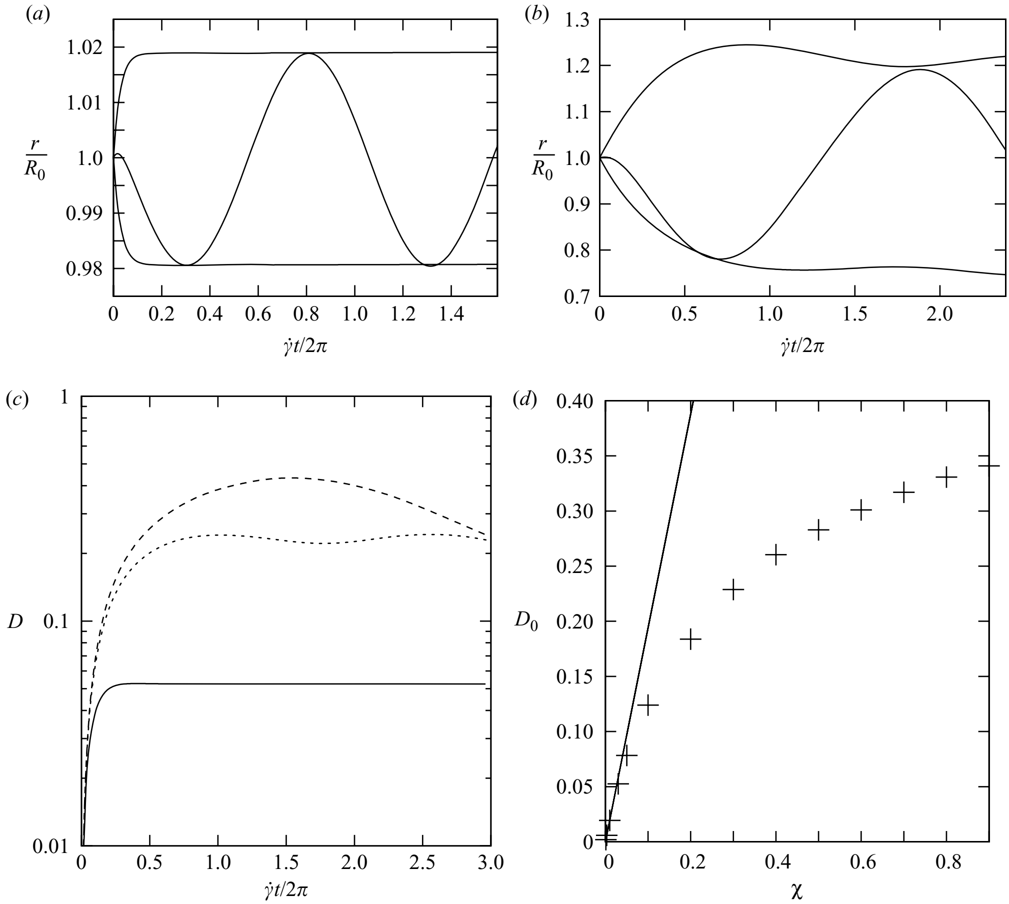

FIGURE 3. Dynamics of an initially spherical capsule in shear flow. (*a*, *b*) Time evolution of maximal and minimal radius and radius of a tracer particle for abruptly starting shear flow at time $t = 0$ for different shear rates $\chi = 0.01$ (*a*), $\chi = 0.3$ (*b*). (*c*) Time evolution of deformation parameter D for different shear rates: $\chi = 0.03$ (continuous), $\chi = 0.3$ (dotted), $\chi = 3$ (dashed line). (*d*) Plot of the stationary deformation parameter D_0 as a function of the dimensionless shear rate χ. For low shear rates the results of the linear theory (equation (4.2), solid line) are approached whereas for higher shear rates deviations are clearly visible. Constant parameters for (*a*)–(*d*): viscosity contrast $\epsilon = 10$, Poisson number $\nu = 0.5$, non-dimensional bending rigidity $\tilde{\kappa} = 0.01$ and spontaneous curvature $\tilde{C}_0 = 1$.

provided by Abkarian *et al.* (2007), who discovered a hysteresis of the transition from tumbling to tank-treading and the reverse transition by increasing or decreasing the shear rate, respectively. We use our spectral method to systematically explore the full phase diagram in a large range in shear rate as well as viscosity contrast. Thus the quantitative accuracy of the reduced model in Skotheim & Secomb (2007) can be tested. While Ramanujan & Pozrikidis (1998) observed the onset of a tumbling motion for low sphericity, owing to the formation of cusp-like instabilities in the shape the simulations never went beyond half a tumbling motion. Grid distortion also required the use of explicit numerical smoothing in more recent simulations (Pozrikidis 2003*b*). Since bending rigidity is included in our method, the formation of cusps can be suppressed, leading to a more stable algorithm. The cutoff at a finite bandwidth in our algorithm also effectively implements numerical smoothing.

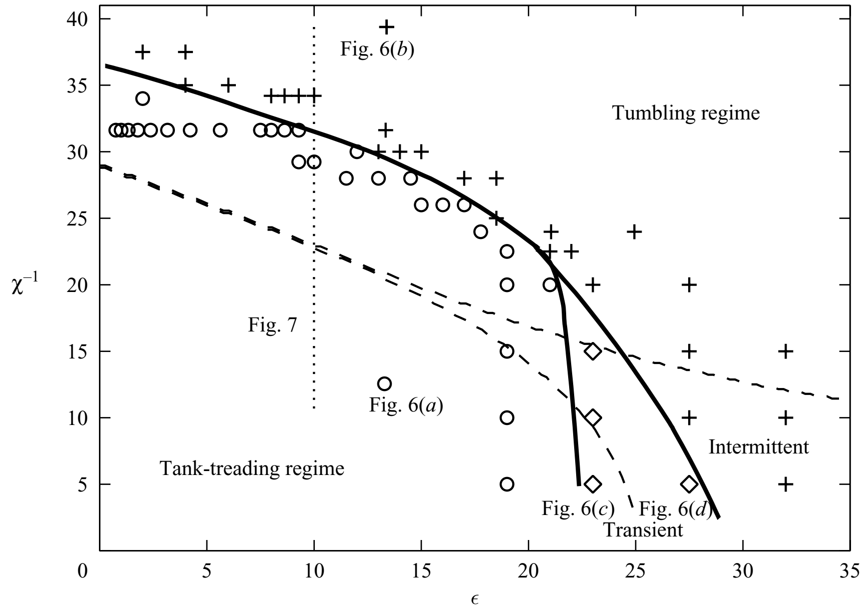

FIGURE 4. Phase diagram of an elastic capsule in shear flow with the tumbling and tank-treading regimes as a function of the viscosity contrast ϵ and the inverse dimensionless shear rate χ^{-1}. The solid line is a guide to the eye separating the tank-treading (circles), tumbling (crosses) and transient region (diamonds) for our simulation. Dashed lines indicate the phase diagram due to Skotheim & Secomb (2007) for the same parameter set. In the region between the dashed lines intermittent motion is predicted. We have not found conclusive evidence for this kind of motion, but rather found transient dynamics from tumbling to tank-treading. The numbers correspond to following figures, where parts of the phase diagram are examined closer. Geometrical parameters: $a_2 = a_3 = 0.9a_1$, elastic parameters: $\nu = 0.333$, $\tilde{\kappa} = 0.01$, $\tilde{C}_0 = 1$.

Nevertheless high-order modes accumulate numerical errors during the simulation run, in particular at large shear rates, thereby limiting the maximum simulation time.

Phase diagram

Our numerical results for the overall phase diagram are summarized in figure 4, where the dynamical behaviour is plotted as a function of the inverse dimensionless shear rate χ^{-1} and the viscosity contrast ϵ. At low shear rate, the hydrodynamic forces are too small to overcome the energy barrier present for a tank-treading motion due to the shape memory effect. Therefore, capsules tumble at low χ, while an oscillating tank-treading behaviour is stable at large χ. We also observe a transient dynamics from tumbling to tank-treading for large viscosity contrast ϵ, which will be discussed below. Although this transient dynamics might be taken as an indication of intermittent motion, we could not find conclusive evidence during the time of our simulation runs. In particular, we never observed a transition from tank-treading to tumbling. Also shown in this figure is the phase diagram for the analytic model by Skotheim & Secomb (2007). The qualitative agreement, apart from the apparent lack of intermittent behaviour, seems to be rather good, given the crude dynamics implemented in the reduced analytical model. Only at large viscosity contrast do pronounced differences in the shape of the phase diagram start to feature. Closer inspection of the data reveals significant oscillations of the axis lengths, which are fixed

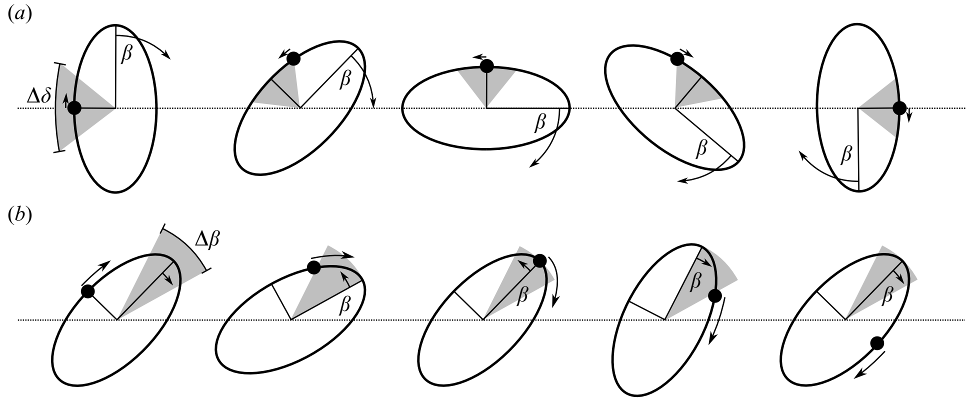

FIGURE 5. Definition of oscillation amplitudes of phase and inclination angle in tumbling and tank-treading states of motion. (*a*) The tumbling state: here the inclination angle β changes monotonically while the phase angle δ oscillates with amplitude $\Delta\delta$ as is indicated by a tracer particle. (*b*) The tank-treading motion, where the inclination angle β oscillates, while the phase angle δ and the tank-treading angle α change monotonically.

in the reduced model. These breathing modes may alter the intermittent character of the capsule motion in the model by Skotheim & Secomb (2007).

For all simulations the deformation remained well within the range of validity of Hooke's law. The extension ratios (see the Appendix) never deviated more than 5% from unity. The results are therefore not susceptible to the specific elastic law in this regime.

Oscillation amplitudes

We now quantify the oscillations in the tank-treading and tumbling state and investigate the transient dynamics. For the definition of inclination β and tank-treading angle α see figure 1. They are defined as the angles between the flow direction and the maximal radius or a marker point, respectively. Initially, these angles are chosen to lie in the interval $[0, \pi[$. To make both $\alpha(t)$ and $\beta(t)$ continuous functions of time, we manually add 2π after a full rotation, thereby keeping the variation of each angle between subsequent time steps as small as possible. As a consequence, the angles can assume values outside the interval $[0, 2\pi[$ at later times. This allows us to count the number of full rotations, which would not be possible if all angles were restricted to $[0, 2\pi[$. The phase shift of a material point away from its elastic minimum

$$\delta(t) \equiv (\alpha(t) - \beta(t)) - (\alpha(0) - \beta(0)) \tag{5.1}$$

is called phase angle.

In the tank-treading regime the inclination angle β oscillates around a stationary value β_0 with amplitude $\Delta\beta$ while the tank-treading angle α or phase angle δ changes monotonically with time (see figure 5). In the tumbling regime, the inclination angle β changes monotonically with time, while the phase angle δ oscillates around a fixed value δ_0 with an oscillation amplitude $\Delta\delta$. Figure 6 shows parametric plots of inclination vs. phase angle for a tumbling and a tank-treading motion, as well as a transition from tumbling to tank-treading. The arrows indicates the direction of time in this plot. In figures 6(*c*) and 6(*d*), one can see the transition from a tumbling motion to an oscillating tank-treading motion near the transition. Despite an intensive search,

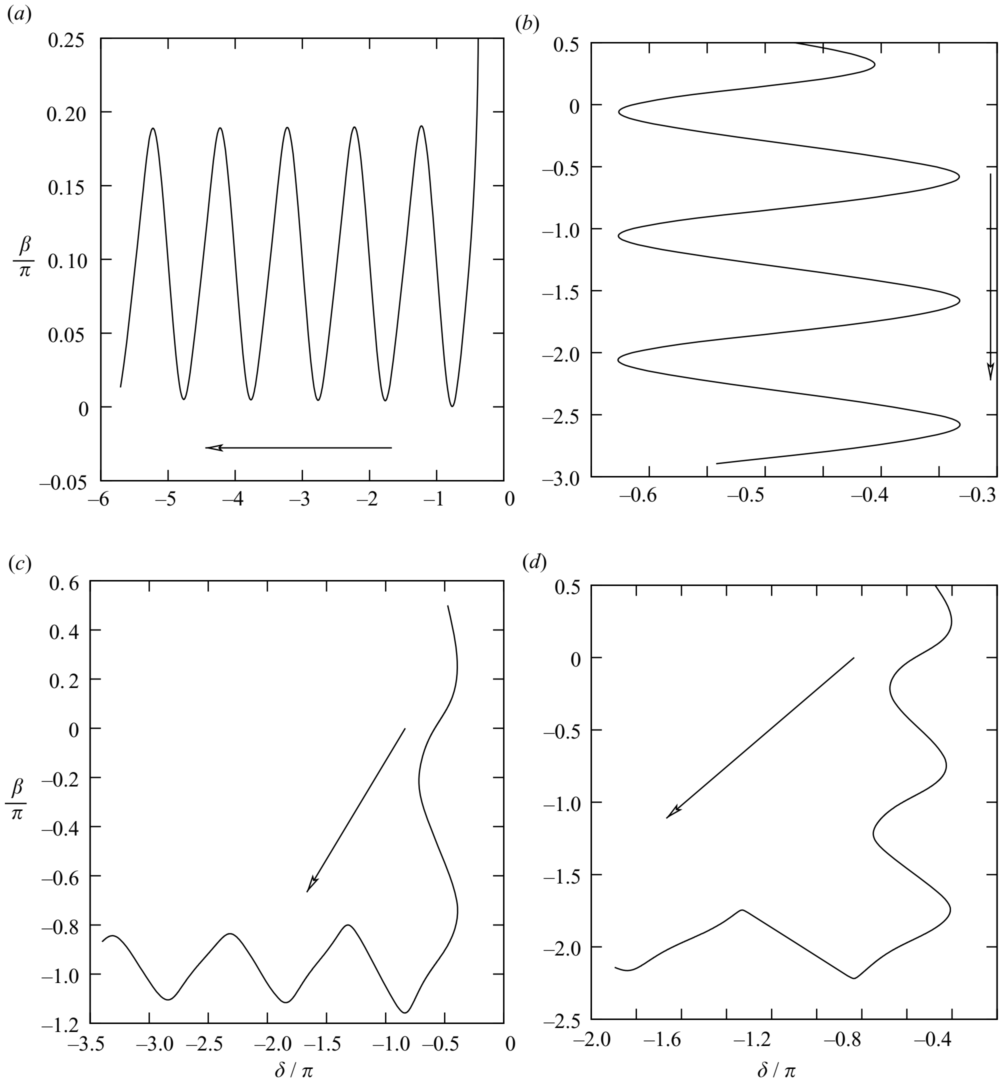

FIGURE 6. Typical plots of inclination angle β vs. phase angle δ for tank-treading, tumbling and transient dynamics. The sites of these plots in the phase diagram are labelled in figure 4 by corresponding numbers. (*a*) Typical tank-treading motion: β oscillates around a stable value, while δ changes monotonically. The arrow denotes the direction in time, viscosity contrast $\epsilon = 13.3$, non-dimensional shear rate $\chi = 0.08$. (*b*) Typical tumbling motion: δ oscillates around a stable value, while β changes monotonically, $\epsilon = 13.3$, $\chi = 0.025$. (*c*, *d*) Typical motions for tumbling to tank-treading transition, $\epsilon = 23$, $\chi = 0.2$ in (*c*) and $\epsilon = 27.5$, $\chi = 0.2$ in (*d*). The remaining parameters are equal to those used in figure 4.

we have not observed the reverse behaviour: a tank-treading capsule never started to tumble. This might indicate that the initial tumbling motion is only transient.

For a fixed viscosity contrast $\epsilon = 10$, figure 7 shows the shear rate dependence of the mean inclination angle β_0 in the tank-treading regime, of the mean phase angle δ_0 in the tumbling regime, and of the oscillation amplitudes in both the tumbling and the tank-treading regime. For low shear rates, in the tumbling regime, the mean phase angle δ_0 and the oscillation amplitude $\Delta\delta$ of the phase angle are plotted as a function

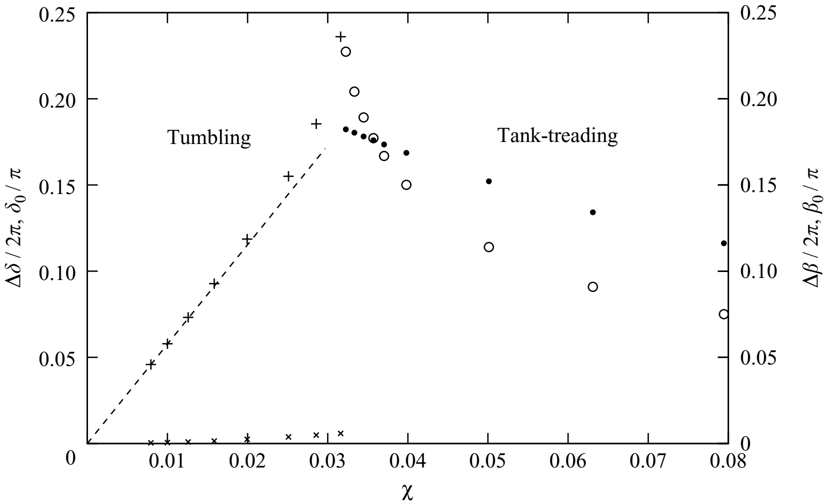

FIGURE 7. Mean phase angle δ_0 (small crosses), mean inclination angle β_0 (small filled circles), and oscillation amplitudes of phase angle $\Delta\delta$ (pluses) and inclination angle $\Delta\beta$ (circles) for different shear rates χ and a constant viscosity contrast $\epsilon = 10$. This cut through the phase diagram with $\epsilon = 10$ is indicated by the dotted line in figure 4. At low shear rates the capsule tumbles with $\Delta\delta < \pi/2$ where the dashed line indicates a linear behaviour for small χ, at higher shear rates the capsule tank-treads with $\Delta\beta < \pi/2$. The remaining parameters are as in figure 4.

of the shear rate. Whereas the mean phase angle depends only weakly on the shear rate, the oscillation amplitude of the phase angle increases for increasing shear rate. For low shear rates, this amplitude grows approximately linearly with the shear rate. When the amplitude reaches approximately $\pi/2$, the capsule starts to tank-tread.

For higher shear rates, in the tank-treading regime, the mean inclination angle β_0 and the oscillation amplitude $\Delta\beta$ of the inclination angle are plotted as a function of χ. With decreasing shear rate, the oscillation amplitude of the inclination angle increases until it reaches approximately $\pi/2$, where the transition to tumbling takes place. The mean inclination angle also increases, but does not reach $\pi/4$. Perhaps surprisingly, the oscillation amplitude can be larger than the mean inclination angle β_0 in the tank-treading regime, implying that the inclination angle is negative for short periods of time.

6. Summary

During the last few years, the dynamics of elastic capsules in linear shear flow has received increasing attention. Theoretical descriptions restricting the capsule deformation to a few degrees of freedom predicted a rich dynamical phase diagram, comprising tank-treading, tumbling and an intermittent motion. While recent experiments have found a hysteresis in the tank-treading to tumbling transition for varying shear rate, direct observations of intermittent behaviour are lacking so far.

To investigate elastic capsule systems, while maintaining complete control over the underlying equations of motion, we implemented a spectral method to numerically solve the equations of motion for a capsule. The capsule deformation is expanded into smooth basis functions, leading to accurate estimates of the membrane forces.

The code is flexible and stable enough to permit simulations for a large range of shear rates and viscosity contrasts between inner and outer fluids.

Using this code, we could quantitatively recover the asymptotically known stationary deformations of initially spherical capsules for low shear rate.

Finally we applied the numerical method to an ellipsoidal capsule system similar to the one discussed by Skotheim & Secomb (2007). We observe a stable tank-treading motion for large shear rate, in which the inclination angle oscillates with twice the tank-treading frequency. At lower shear rate, or higher viscosity contrast, the capsule starts to tumble. We systematically explored the capsule dynamics over a wide range of viscosity ratios and shear rates. The resulting phase diagram is qualitatively similar to the theoretical predictions made by Skotheim & Secomb (2007), with the exception of intermittent dynamics: while dynamic transitions from tumbling to a stable tank-treading motion were observed, the reverse transition could not be observed. An analysis of the results suggests that the tumbling motion is only transient in this part of the phase diagram.

Much longer simulation runs and a more detailed analysis near the presumed intermittency region are needed to decide whether intermittent motion is merely an artifact of the reduced dynamics employed by Skotheim & Secomb (2007). Differences from the phase diagram at large viscosity ratios are probably due to the restriction to a fixed capsule shape in the reduced model.

In conclusion, the spectral method developed in this work is a stable and accurate complement to existing numerical methods. It allows the systematic exploration of capsule dynamics over a wide range of material constants. Theoretical predictions of the phase diagram of ellipsoidal capsules are qualitatively confirmed, although quantitative differences exist, especially for large viscosity ratios. The nature of predicted intermittent behaviour warrants further investigation.

Financial support of the DFG within the priority programme SPP 1164 “Nano- and Microfluidics” is gratefully acknowledged.

Appendix. Differential geometry for deformed capsules

We first recall some definitions of differential geometry that can be found in Frankel (2004) and Marsden & Hughes (1983). We cover the two-dimensional surface with a coordinate net as outlined in § 2, where the coordinates (ϑ, φ) label the material points. The location of the surface at time t is given by the shape function $\boldsymbol{r}(\vartheta, \varphi; t)$. The basis vectors, defined by

$$\boldsymbol{e}_i \equiv \partial_i \boldsymbol{r}, \quad i = \vartheta, \varphi, \tag{A 1}$$

span the tangent planes and induce the outward-pointing normal unit vector

$$\boldsymbol{n} \equiv \frac{1}{|\boldsymbol{e}_\vartheta \times \boldsymbol{e}_\varphi|} \boldsymbol{e}_\vartheta \times \boldsymbol{e}_\varphi . \tag{A 2}$$

They also define the metric tensor $\boldsymbol{g}$ with covariant components

$$g_{ij} \equiv \boldsymbol{e}_i \cdot \boldsymbol{e}_j , \tag{A 3}$$

where we use the ordinary three-dimensional Euclidian scalar product. The inverse metric tensor $\boldsymbol{g}^{-1}$ with contravariant components is given by

$$g^{ij} g_{jk} \equiv \delta^i{}_k , \tag{A 4}$$

where Einstein's sum convention is employed. The determinant of the metric tensor

$$g \equiv \det \boldsymbol{g} \tag{A 5}$$

is connected to the basis vectors via

$$\sqrt{g} = |\boldsymbol{e}_\vartheta \times \boldsymbol{e}_\varphi| \; . \tag{A 6}$$

The area of an infinitesimal patch with width $\mathrm{d}\vartheta$ and length $\mathrm{d}\varphi$ in Lagrange coordinates is given by

$$\mathrm{d}a = \sqrt{g}\mathrm{d}\vartheta d\varphi \, . \tag{A 7}$$

The curvature tensor $\boldsymbol{k}$, defined by

$$k_{ij} \equiv \boldsymbol{e}_i \cdot \partial_j \boldsymbol{n} = -\boldsymbol{n} \cdot \partial_i \boldsymbol{e}_j \; , \tag{A 8}$$

measures how the normal vector $\boldsymbol{n}$ changes its direction on moving along the membrane. Its eigenvalues $k_{1,2}$ are called principle curvatures and are the inverse radii of the principle curvature circles. The trace and determinant of the curvature tensor define mean H and Gaussian curvature K, respectively. They serve as scalar invariants of the curvature tensor and can be expressed by the sum and the product of the principle curvatures

$$2H \equiv \mathrm{tr}\,\boldsymbol{k} = g^{ij} k_{ji} = k_1 + k_2 \, , \quad K \equiv \det \boldsymbol{k} = k_1 k_2 \, . \tag{A 9}$$

In order to describe a deformation and an elastic response, an unstressed reference shape $\boldsymbol{R}(\vartheta, \varphi)$ must be specified as was mentioned in § 2. The corresponding basis vectors $\boldsymbol{E}$, normal vector $\boldsymbol{N}$ and metric $\boldsymbol{G}$ are defined analogously.

The Lagrangian strain tensor $\boldsymbol{\varepsilon}$ with covariant components

$$\varepsilon_{ij} \equiv \tfrac{1}{2}(g_{ij} - G_{ij}), \quad i = \vartheta, \varphi, \tag{A 10}$$

measures the change in length elements of the membrane upon deformation (Marsden & Hughes 1983).

At each point of the reference membrane there are two orthogonal directions, called principle extension directions, for which the deformation is maximal and minimal. The corresponding deformed line elements along these directions remain orthogonal and have a stretched length given by the so-called extension ratios λ_i measured in units of the undeformed line elements.

An infinitesimal material patch on the reference shape with area $\mathrm{d}A = \sqrt{G}\mathrm{d}\vartheta\mathrm{d}\varphi$ will deform into the area element $\mathrm{d}a = \sqrt{g}\mathrm{d}\vartheta\mathrm{d}\varphi$ on the current shape. The surface dilation J is therefore given by the product of the extension ratios

$$J \equiv \frac{\mathrm{d}a}{\mathrm{d}A} = \sqrt{\frac{g}{G}} = \lambda_1 \lambda_2 \, . \tag{A 11}$$

All scalar deformation quantities can be expressed by the extension ratios or equivalently by the eigenvalues of the Lagrangian strain tensor ε_i, which measure the difference of the extension ratios from unity

$$\varepsilon_i \equiv \tfrac{1}{2}\left(\lambda_i^2 - 1\right) \, . \tag{A 12}$$

REFERENCES

Abkarian, M., Faivre, M. & Viallat, A. 2007 Swinging of red blood cells under shear flow. *Phys. Rev. Lett.* **98**, 188302.

ABKARIAN, M., LARTIGUE, C. & VIALLAT, A. 2002 Tank treading and unbinding of deformable vesicles in shear flow: Determination of the lift force. *Phys. Rev. Lett.* **88**, 068103.

BARTHÈS-BIESEL, D. 1980 Motion of a spherical microcapsule freely suspended in a linear shear flow. *J. Fluid Mech.* **100**, 831.

BARTHÈS-BIESEL, D., DIAZ, A. & DHENIN, E. 2002 Effect of constitutive laws for two-dimensional membranes on flow-induced capsule deformation. *J. Fluid Mech.* **460**, 211.

BARTHÈS-BIESEL, D. & RALLISON, J. M. 1981 The time-dependent deformation of a capsule freely suspended in a linear shear-flow. *J. Fluid Mech.* **113**, 251.

BEAUCOURT, J., BIBEN, T. & MISBAH, C. 2004*a* Optimal lift force on vesicles near a compressible substrate. *Europhys. Lett.* **67**, 676.

BEAUCOURT, J., RIOUAL, F., SEON, T., BIBEN, T. & MISBAH, C. 2004*b* Steady to unsteady dynamics of a vesicle in a flow. *Phys. Rev.* E **69**, 011906.

BIBEN, T. & MISBAH, C. 2003 Tumbling of vesicles under shear flow within an advected-field approach. *Phys. Rev.* E **67**, 031908.

BOYD, J. P. 2001 *Chebyshev and Fourier Spectral Methods*, 2nd edn. Dover.

BRINK, D. M. & SATCHLER, G. R. 1968 *Angular Momentum*, 2nd edn. Clarendon.

CANTAT, I. & MISBAH, C. 1999 Lift force and dynamical unbinding of adhering vesicles under shear flow. *Phys. Rev. Lett.* **83**, 880.

CHANG, K. S. & OLBRICHT, W. L. 1993 Experimental studies of the deformation and breakup of a synthetic capsule in steady and unsteady simple shear-flow. *J. Fluid Mech.* **250**, 609.

FINKEN, R. & SEIFERT, U. 2006 Wrinkling of microcapsules in shear flow. *J. Phys.: Condens. Matter* **18**, L185.

FISCHER, T. M. 2004 Shape memory of human red blood cells. *Biophys. J.* **86**, 3304.

FRANKEL, T. 2004 *The Geometry of Physics*, 2nd edn. Cambridge University Press.

DE HAAS, K. H., BLOM, C., VAN DEN ENDE, D., DUITS, M. H. G. & MELLEMA, J. 1997 Deformation of giant lipid bilayer vesicles in shear flow. *Phys. Rev.* E **56**, 7132.

HAPPEL, J. & BRENNER, H. 1983 *Low Reynolds Number Hydrodynamics*, 1st edn. Martinus Nijhoff.

HEALY, D. M., ROCKMORE, D. N., KOSTELEC, P. J. & MOORE, S. 2003 FFTs for the 2-sphere-improvements and variations. *J. Fourier Anal. Applics.* **9**, 341.

HELFRICH, W. 1973 Elastic properties of lipid bilayers–theory and possible experiments. *Z. Naturforsch.* (C) **28**, 693.

KANTSLER, V., SEGRE, E. & STEINBERG, V. 2007 Vesicle dynamics in time-dependent elongation flow: Wrinkling instability. *Phys. Rev. Lett.* **99**, 178102.

KANTSLER, V. & STEINBERG, V. 2005 Orientation and dynamics of a vesicle in tank-treading motion in shear flow. *Phys. Rev. Lett.* **95**, 258101.

KANTSLER, V. & STEINBERG, V. 2006 Transition to tumbling and two regimes of tumbling motion of vesicles in shear flow. *Phys. Rev. Lett.* **96**, 036001.

KELLER, S. R. & SKALAK, R. 1982 Motion of a tank-treading ellipsoidal particle in a shear-flow. *J. Fluid Mech.* **120**, 27.

KRAUS, M., WINTZ, W., SEIFERT, U. & LIPOWSKY, R. 1996 Fluid vesicles in shear flow. *Phys. Rev. Lett.* **77**, 3685.

LAMB, H. 1932 *Hydrodynamics*, 6th edn. Cambridge University Press.

LEBEDEV, V. V., TURITSYN, K. S. & VERGELES, S. S. 2007 Dynamics of nearly spherical vesicles in an external flow. *Phys. Rev. Lett.* **99**, 218101.

LEYRAT-MAURIN, A. & BARTHES-BIESEL, D. 1994 Motion of a deformable capsule through a hyperbolic constriction. *J. Fluid Mech.* **279**, 135.

LEYRAT-MAURIN, A., DROCHON, A. & BARTHES-BIESEL, D. 1993 Flow of a capsule through a constriction - application to cell filtration. *J. Phys. Paris* III **3**, 1051.

LI, X. Z., BARTHÈS-BIESEL, D. & HELMY, A. 1988 Large deformations and burst of a capsule freely suspended in an elongational flow. *J. Fluid Mech.* **187**, 179.

LORZ, B., SIMSON, R., NARDI, J. & SACKMANN, E. 2000 Weakly adhering vesicles in shear flow: Tanktreading and anomalous lift force. *Europhys. Lett.* **51**, 468.

MARSDEN, J. E. & HUGHES, T. J. R. 1983 *Mathematical Foundations of Elasticity*. Prentice-Hall.

MISBAH, C. 2006 Vacillating breathing and tumbling of vesicles under shear flow. *Phys. Rev. Lett.* **96**, 28104.

Mohandas, N. & Evans, E. 1994 Mechanical properties of the red cell membrane in relation to molecular structure and genetic defects. *Annu. Rev. Biophys. Biomolec. Struct.* **23**, 787.

Morse, P. M. & Feshbach, H. 1953 *Methods of Theoretical Physics*. McGraw-Hill.

Noguchi, H. & Gompper, G. 2004 Fluid vesicles with viscous membranes in shear flow. *Phys. Rev. Lett.* **93**, 258102.

Noguchi, H. & Gompper, G. 2005 Shape transitions of fluid vesicles and red blood cells in capillary flows. *Proc. Natl Acad. Sci. USA* **102**, 14159.

Noguchi, H. & Gompper, G. 2007 Swinging and tumbling of fluid vesicles in shear flow. *Phys. Rev. Lett.* **98**, 128103.

Pozrikidis, C. 1995 Finite deformation of liquid capsules enclosed by elastic membranes in simple shear-flow. *J. Fluid Mech.* **297**, 123.

Pozrikidis, C. 2001 Interfacial dynamics for Stokes flow. *J. Comput. Phys.* **169**, 250.

Pozrikidis, C. 2003*a* *Modelling and Simulation of Capsules and Biological Cells*. Chapman & Hall/CRC.

Pozrikidis, C. 2003*b* Numerical simulation of the flow-induced deformation of red blood cells. *Ann. Biomed. Engng* **31**, 1194.

Pozrikidis, C. 2006 A spectral collocation method with triangular boundary elements. *Engng Anal. Bound. Elem.* **30**, 315.

Ramanujan, S. & Pozrikidis, C. 1998 Deformation of liquid capsules enclosed by elastic membranes in simple shear flow: Large deformations and the effect of fluid viscosities. *J. Fluid Mech.* **361**, 117.

Rioual, F., Biben, T. & Misbah, C. 2004 Analytical analysis of a vesicle tumbling under a shear flow. *Phys. Rev.* E **69**, 061914.

Rochal, S. B., Lorman, V. L. & Mennessier, G. 2005 Viscoelastic dynamics of spherical composite vesicles. *Phys. Rev.* E **71**, 021905.

Rose, M. E. 1957 *Elementary Theory of Angular Momentum*. Wiley.

Seifert, U. 1999*a* Fluid dynamics in hydrodynamic force fields: Formalism and an application to fluctuating quasispherical vesicles in shear flow. *Eur. Phys. J.* B **8**, 405.

Seifert, U. 1999*b* Hydrodynamic lift on bound vesicles. *Phys. Rev. Lett.* **83**, 876.

Skotheim, J. M. & Secomb, T. W. 2007 Red blood cells and other nonspherical capsules in shear flow: Oscillatory dynamics and the tank-treading-to-tumbling transition. *Phys. Rev. Lett.* **98**, 078301.

Sukumaran, S. & Seifert, U. 2001 Influence of shear flow on vesicles near a wall: A numerical study. *Phys. Rev.* E **64**, 11916.

Swarztrauber, P. N. & Spotz, W. F. 2004 Spherical harmonic projectors. *Math. Comput.* **73**, 753.

Vlahovska, P. M. & Gracia, R. S. 2007 Dynamics of a viscous vesicle in linear flows. *Phys. Rev.* E **75**, 016313.

Walter, A., Rehage, H. & Leonhard, H. 2001 Shear induced deformation of microcapsules: shape oscillations and membrane folding. *Colloid Surf.* A **183–185**, 123.

Wang, Y. C. & Dimitrakopoulos, P. 2006 A three-dimensional spectral boundary element algorithm for interfacial dynamics in Stokes flow. *Phys. Fluids* **18**.

Watanabe, N., Kataoka, H., Yasuda, T. & Takatani, S. 2006 Dynamic deformation and recovery response of red blood cells to a cyclically reversing shear flow: Effects of frequency of cyclically reversing shear flow and shear stress level. *Biophys. J.* **91**, 1984.